# Post-main Sequence Evolution

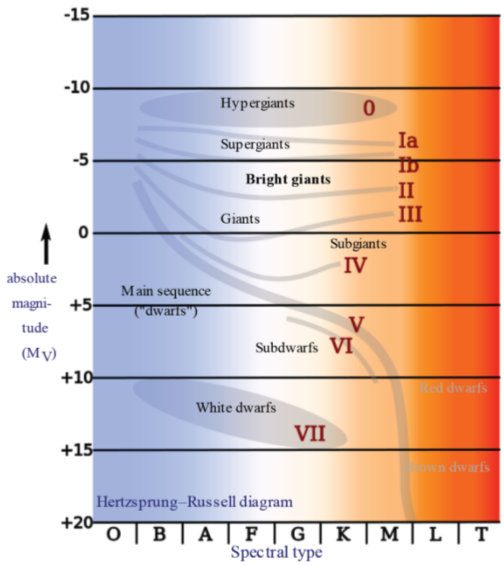


http://en.wikipedia.org/wiki/File:HR-diag-no-text-2.svg

## Hypergiants

luminosity class 0; excessive mass loss

## Supergiants

Ia luminous supergiants;
Ib supergiants; $\mathrm{Ia}^+ = 0$

## Subgiants

luminous class IV; between MS turn-off and the red giant branch

## Dwarfs

luminosity class V = MS stars

## Subdwarfs (sd)

luminosity class VI, 1.5 to 2 mag lower than MS; lower metallicity

2

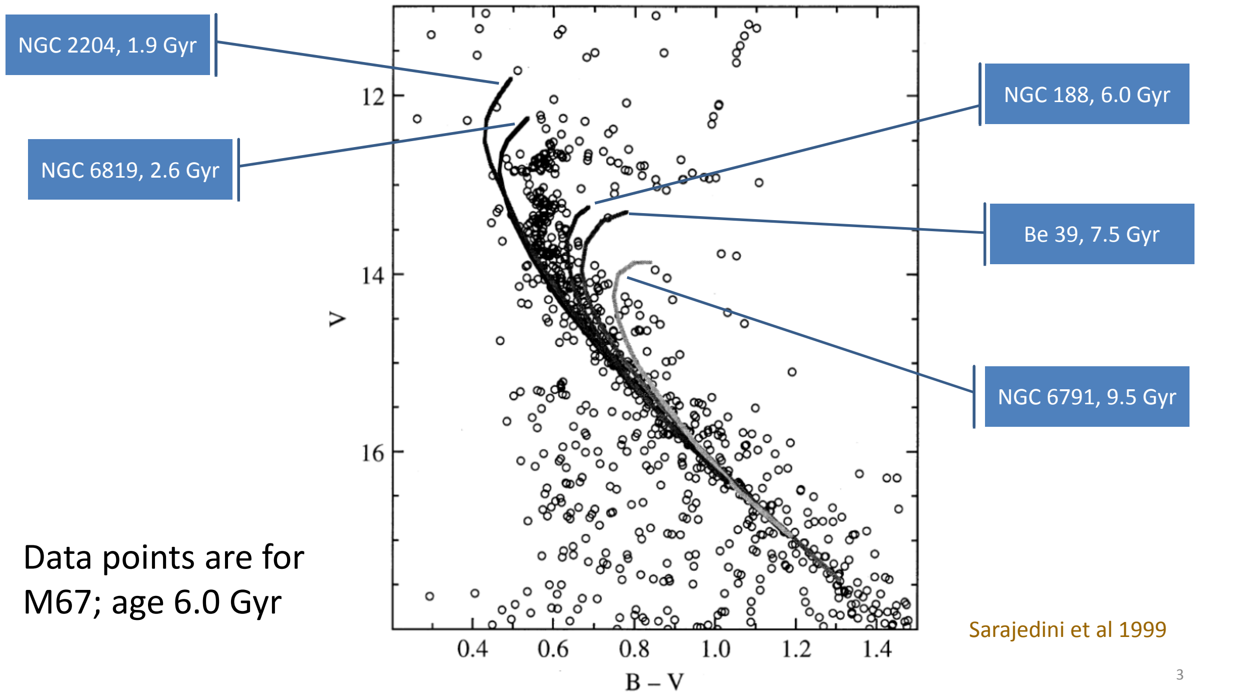


# Mass Loss during Stellar Evolution

- Stars lose mass at all evolutionary stages.
- <u>Pre-main sequence</u>: protostellar (bipolar) outflows
  YSO jets, (star/disk) winds
- <u>Main sequence</u>: solar wind $\dot{\mathcal{M}} = 10^{-14}\ M_\odot\ \mathrm{yr}^{-1}$
  For $\tau_{\mathrm{MS}} \approx 10^{10}$ yr → $\tau_{\mathrm{loss,MS}} \approx 10^{-4}\ M_\odot$
  Some stars, e.g., WR stars $\dot{\mathcal{M}} = 10^{-5}\ M_\odot\ \mathrm{yr}^{-1}$
- <u>Post-main sequence</u>: $R \uparrow \longrightarrow g \downarrow$, and $P_{\mathrm{rad}} \uparrow \Longrightarrow\ \dot{\mathcal{M}} \uparrow$

4

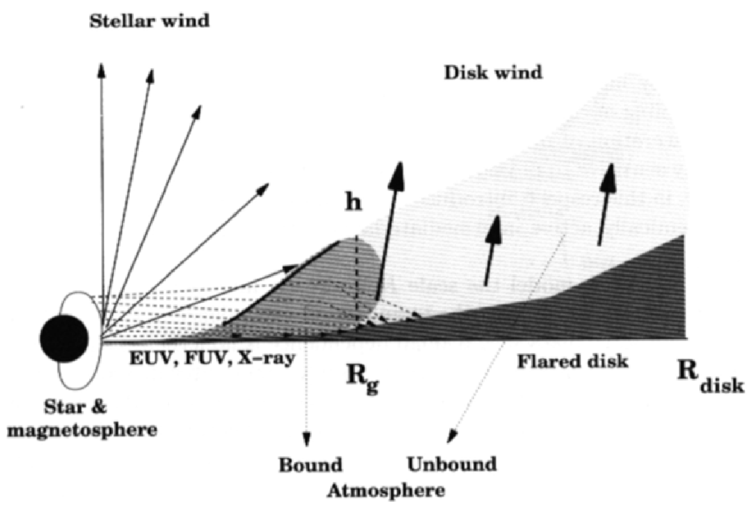


**Fig. 7.6.** Schematic representation of an irradiated flared disk. Below the radius $R_g$ where matter remains bound by the gravity of the central star an optically thin atmosphere develops. Above this radius flared matter may escape and form some kind of slow wind. Adapted from Hollenbach et al. [403].

Schulz

5

- For a stationary, isotropic wind, the mass loss rate

$$\dot{\mathcal{M}} = 4\,\pi r^2\,\rho(r)\,\frac{\mathrm{dr}}{\mathrm{d}t} = 4\,\pi r^2\,\rho(r)\,v(r)$$

$v(r)$: velocity law

- $v(r)\uparrow$, at $r \to \infty$, $v_\infty \equiv v(r \to \infty)$ terminal velocity

  Often $v(r) \approx v_0 + (v_\infty - v_0)\left(1 - \frac{R_*}{r}\right)^{\beta}$, where

  $v_0 = v(R_*)$ at photosphere

- $\beta \leq 1, v \to v_\infty$ gradually $\quad \beta \geq 1, v \to v_\infty$ slowly
- For hot stars, $\beta \approx 0.8$. Cool stars experience slower acceleration, so have larger $\beta$.

6

$$\dot{\mathcal{M}} = 4\,\pi r^2\,\rho(r)\,v(r)$$ mass conservation

$$\ddot{r} = -\frac{1}{\rho}\frac{\mathrm{d}P}{\mathrm{d}r} - \frac{GM}{r^2} = \frac{\mathrm{d}v}{\mathrm{d}t} = \frac{\mathrm{d}v}{\mathrm{d}r}\frac{\mathrm{d}r}{\mathrm{d}t} = v\frac{\mathrm{d}v}{\mathrm{d}r}$$ momentum conservation

Massive stars → radiation pressure → outer atmosphere expands supersonically → winds driven by spectral-line opacity in UV.

7

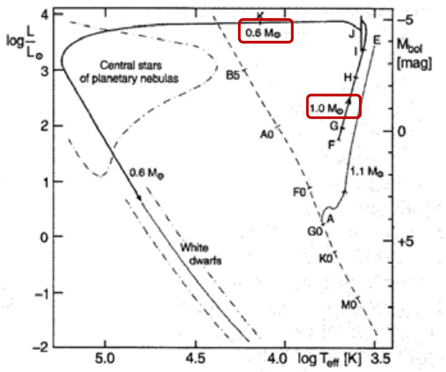


**Fig. 8.8.** The evolutionary paths in the Hertzsprung–Russell diagram of Population I stars having 1.0 $\mathcal{M}_\odot$ and 1.1 $\mathcal{M}_\odot$, from central hydrogen burning (A) to the helium flash (E), without taking mass losses into account. After A. V. Sweigart and P. G. Gross (1978). The ejection of a mass of 0.1 $\mathcal{M}_\odot$ during the helium flash was assumed. The further evolution of the star of 1.0 $\mathcal{M}_\odot$ was calculated taking the mass loss according to (7.105) into account, after D. Schönberner (1979). F → G: the asymptotic giant branch; only one of the thermal pulses (helium flashes) which occur after I is drawn in, at J. The mass loss becomes important at H and leads to a final mass of 0.6 $\mathcal{M}_\odot$, which is reached at K

**Mass loss (Reimers 1975)**

$$\dot{M} \approx 4\times10^{-13}\,\frac{L/L_\odot}{(g/g_\odot)\;(R/R_\odot)}\;[\mathrm{M_\odot\;yr^{-1}}]$$

$$g = GM/R^2$$

Sun now $\dot{M} \approx 2\times10^{-14}\ \mathrm{M_\odot\ yr^{-1}}$

Cool supergiant $\dot{M} \approx 10^{-7}$ to $10^{-5}\ \mathrm{M_\odot\ yr^{-1}}$

Unsöld

8

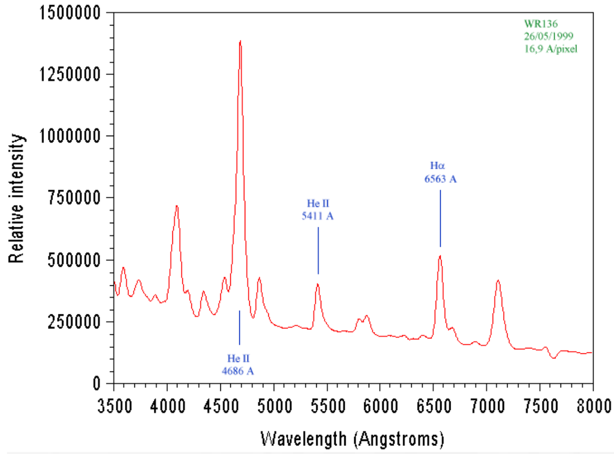


WR stars

$T_{eff} \sim 25,000$ to $50,000$ K

Evolved massive ($\gtrsim 20 M_\odot$) stars

Wind $\sim 2000 \, km \, s^{-1}$

$\dot{m} \sim 10^{-5} M_\odot \, yr^{-1}$

Spectrum of a Wolf-Rayet Star

$O(\rightarrow WN) \rightarrow LBV \rightarrow \begin{matrix} WN \\ WC \end{matrix}$

$\rightarrow SN\,Ib,c$

9

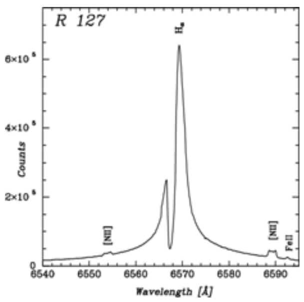


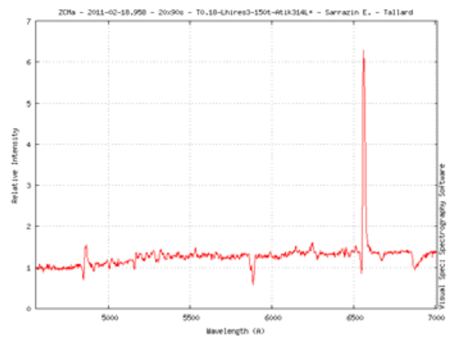


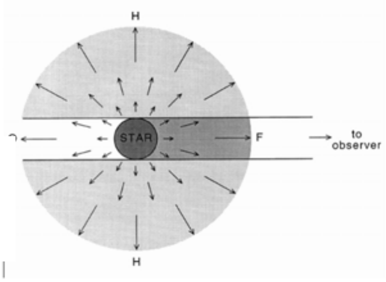


**P Cygni profile** of a spectral line
--- a blue-shifted absorption
superimposed on an emission line
→ **mass loss** (cool gas toward us)

Lamers and Cassinelli, *Introduction to Stellar Winds*, Cambridge, 1999

10

## P Cygni stars

- **Higher mass-loss rate,** $> 10^{-5}\,\mathrm{M}_\odot\,\mathrm{yr}^{-1}$
- **Lower terminal velocity,** $v_\infty < 10^{2.5}\,\mathrm{km\,s}^{-1}$
- **Higher wind density,** $n_H > 10^{10}\,\mathrm{cm}^{-3}$ **at 2** $R_*$

**than normal stars (Lamers 1986).**

11

## Effects of metallicity

RGB for a Pop II 1.2 $\mathrm{M}_\odot$ star

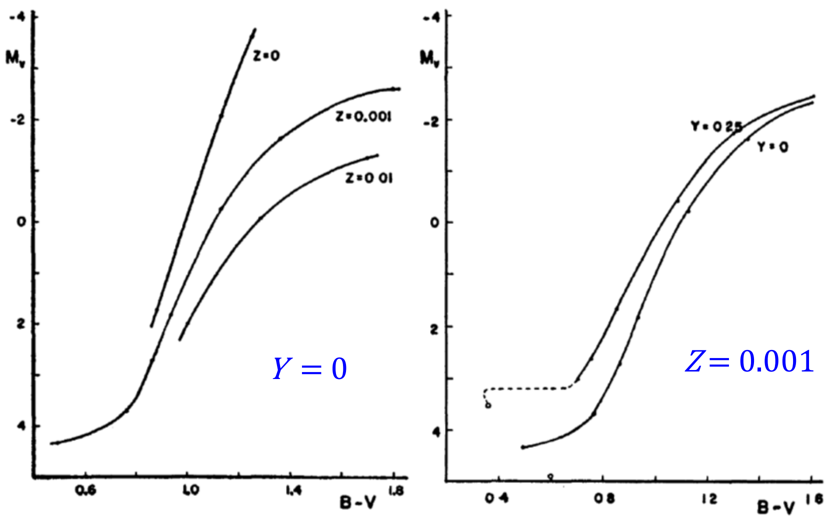


Demarque & Geisler (1963)

12

Next Tuesday (May 30) is a holiday, again.

A make-up class on June 5 (Monday) at 3 pm? June 7 (Wednesday) at 3 pm?

13

## Stellar Pulsation

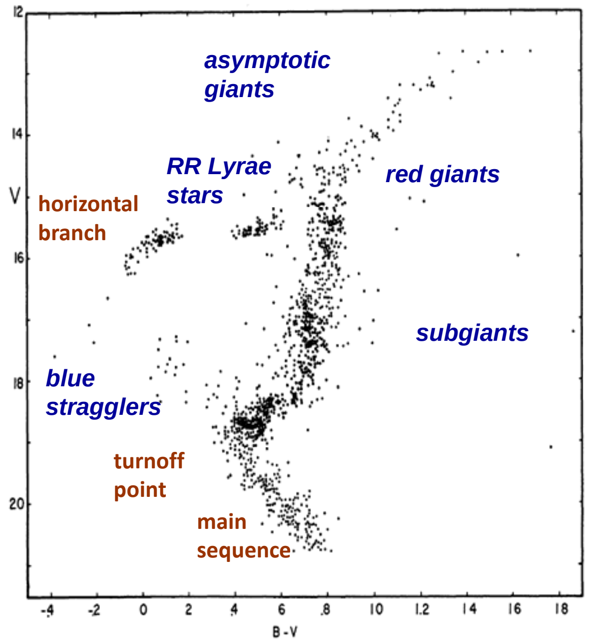


FIG. 5.—Color-magnitude diagram for M3 stars in the arguments $V$ and $B - V$

15

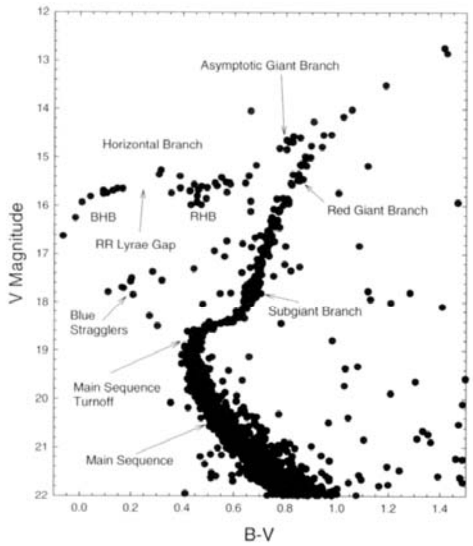


Figure 5.26 A color-magnitude (H–R) diagram of the globular cluster M3, with features mentioned in the text pointed out. Data from Rey et al. (2001).

16

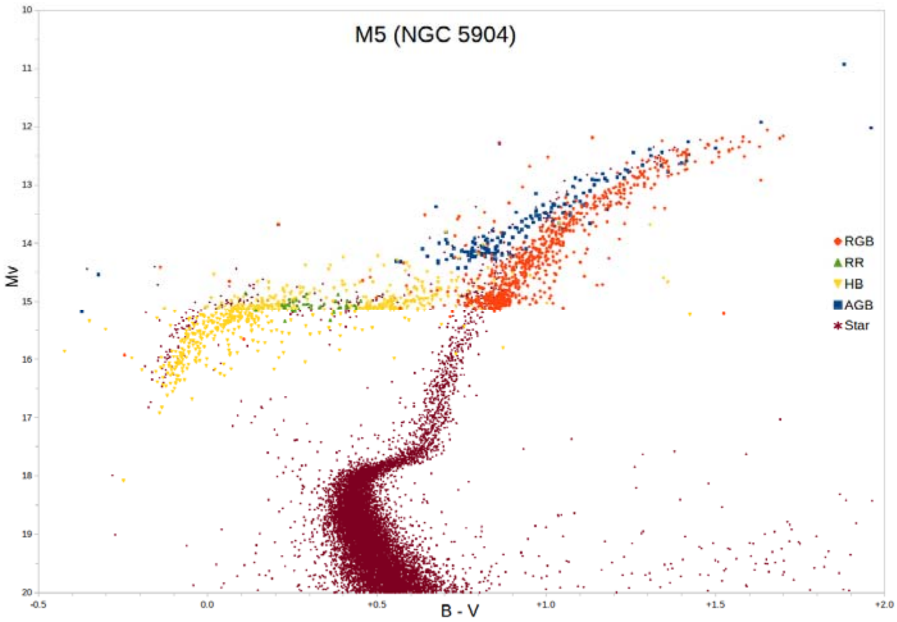


https://en.wikipedia.org/wiki/Subgiant#/media/File:M5_colour_magnitude_diagram.png

17

# Stellar Variability

- Time to transmit a perturbation of pressure changes across the star

$$t_{\text{vib}} \sim \frac{2R}{\bar{v_s}} \quad \text{where} \quad v_s = \sqrt{\gamma \frac{P_g}{\rho}}$$

$\gamma = c_P/c_V = 5/3$ for monatomic gas.

- Virial theorem, $2K + \Omega = 0$, $\therefore$ $\quad v_s^2 = \frac{GM}{R}$

$$\boxed{t_{\text{vib}} \sim \frac{2R}{\sqrt{GM/R}} \sim \frac{1}{\sqrt{G\rho}}}$$ cf. free-fall time

18

## Approximate Relation between Stellar Density, Pulsation and Minimum Rotational Period

| Star | Density g cm$^{-3}$ | $t_{vib}$ sec | $t_{rot,\ min}$ sec |
|---|---|---|---|
| Neutron star | $10^{15}$ | $10^{-4}$ | $3 \times 10^{-4}$ |
| White Dwarf | $10^{7}$ | 1 | 3 |
| RR Lyrae star | $10^{-2}$ | $10^{4.5}$ | $10^{5}$ |
| Cepheid Variable | $10^{-6}$ | $10^{6.5}$ | $10^{7}$ |

$t$ (Crab Nebula) ~ 33 ms → cannot be a white dwarf

- **Rotational Variation** --- sub-seconds .. weeks
- **Pulsational Variation** --- hours .. weeks
- **Orbital (Eclipsing Binaries)** --- hours .. days

19

Valve mechanism (Eddington)

- Heating → P↑ → expansion → cooling
  ∴ Self-regulated stability
- Absorption of radiation
- Usually $\kappa \propto T^{-n}$
  ∴ Heating → (IF) T↑ → κ↓ → cooling
- contraction → releases energy
  expansion → absorbs energy

Normally T↗ → κ↘

Recall Kramers opacity

20

κ mechanism — a partially ionized layer to absorb energy during compression (and release energy during expansion)

In stars, there are 2 ionization zones

— $T \sim (1-1.5) \times 10^4$ K hydrogen ionization zone

HI → HII , HeI → HeII

— $T \sim (4-5) \times 10^4$ K

HeII → HeIII helium ionization zone

But if there is an ionization layer, e.g., $He^+ \rightarrow He^{++}$

T ↗ → κ ↗
energy trapped
→ expansion

Energy escaped
→ Contraction

→ pulsation

21

Depths of ionization zones

e.g. $T_{eff} \gtrsim 7500$ K , zones near surface

→ not enough mass available to drive the oscillation.

$T_{eff} \gtrsim 5500$ K , zones deeper

⇒ significant pulsation

$T_{eff} < 5500$ K , convective outer layer

→ pulsation suppresses

∴ $T_{eff} \sim 5500 - 7500$ K for pulsation to take place. Instability "strip"

There is a certain surface temperature range for stellar pulsation …

22

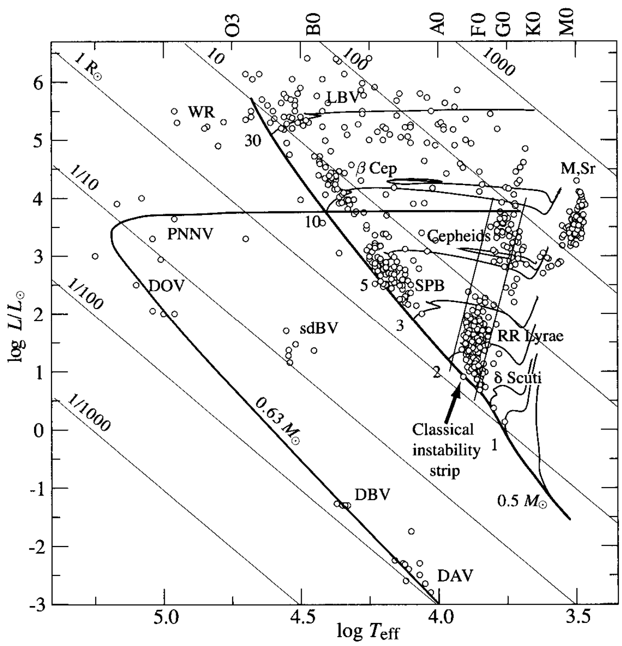


Figure 4.9. Examples of various types of pulsating variable stars plotted as small circles on the Hertzsprung–Russell diagram. The dark line to the right is the main sequence with evolutionary tracks branching off to the right for different stellar masses. The ultimate evolutionary track of a star that ends its life as a compact star of 0.63 $M_\odot$ is shown. It moves leftward through the planetary nebulae nuclei variables (PNNV) and then downward as a cooling white dwarf, passing through regions of pulsational instability sequentially classified as DOV, DBV, and DAV (DAV = Dwarf + type/temperature A + Variable). Other types of intrinsic variables are shown: $\beta$ Cephei stars, Mira (M), Semiregular (Sr), luminous blue (LBV), Wolf–Rayet (WR), slowly pulsating B stars (SPB), and subdwarf B stars (sdBV). The *classical instability strip* is shown as two parallel lines encompassing Cepheid, RR Lyrae, and $\delta$ Scuti variables; if extended, it intersects the pulsating DAV stars. The thin lines represent loci of constant radius. [Provided by A. Gautschy; see Gautschy H. Saio, *ARAA* **33**, 77 (1995)]

Bradt "Astrophycs Processes"

23

Normally, $T \uparrow \Rightarrow \kappa \downarrow$

plays a role also in red giants

Core $\rightarrow$ increased energy output

Envelope $\rightarrow$ expansion, cooling $\rightarrow \kappa \uparrow$

$\Rightarrow$ Red giants have convective envelopes.

cf PMS Hayashi tracks

The envelope extends from just outside of the H-burning shell to the surface.

$\rightarrow$ 'Dredge-up' of processed material from deep interior to surface

24

e.g., observations of heavy elements or
isotope ratios in evolved stars different
from (enrichment) young stars
(in a star cluster)

⇒ Evidence of stellar evolution
〃 of nuclear reactions.



Convection → chemical mixing

Much more efficient than the slow change of chemical composition produced by nuclear reaction.

In a convection region, $\frac{\partial X_i}{\partial m} = 0$

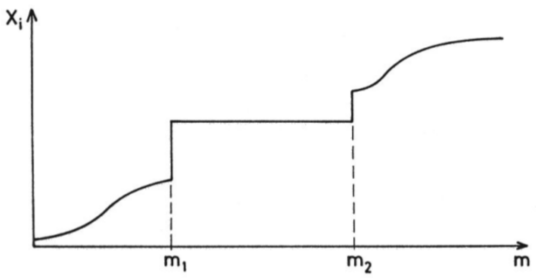


**Fig. 8.1.** The abundances $X_i$ are smeared out owing to rapid mixing inside a convection zone extending from $m_1$ to $m_2$. At these borders $X_i$ can be discontinuous

Kippenhahn & Weigert

## The Dredge-ups

When H shell burning begins, the He core contracts and heats up, making the shell burn furiously. The input of energy forces the envelope to expand and the star moves up the "red giant branch" (RGB). But the furiously burning shell runs on the CNO cycle and now the envelope becomes convective because of the low temperature, high opacity, and high temperature gradient, and processed material from the core mixes for the first time with the envelope. We call this the first dredge-up which should be visible in the spectrum of the photosphere as an increase in N at the expense of C and O.

27

For stars more than half a solar mass, the (gravitationally) contracting and heating He core will reach ignition temperature for triple alpha, and the star will (after a possibly traumatic He-flash start) begin life on the "helium burning main sequence". When the He is exhausted in the core (the H-burning shell never provides enough He to keep the core going very long) the He begins shell burning, and now the star rapidly moves up **the AGB, the Asymptotic Giant Branch**. Now begins a **second dredge-up** where for the first time new elements (C N and O) appear in the star's photosphere. The triple alpha shell is really unstable and generates thermal pulses rather than a clean burn. The C core is nearly degenerate at the C-He boundary. The boundary shrinks, heats up, triple alpha starts, pulses, and the explosion may shut

28

itself down. The pulse is quite muffled by the outer layers of the star. But during a pulse the process can actually initiate more complicated fusion processes including neutron generation which can synthesize heavier elements. So for the first time new elements can be dredged up during the AGB phase of stellar evolution. Now these giant stars all have associated strong stellar winds and so can contribute to the chemical evolution of the cosmos.

29

But why wait for a dredge-up? Really massive O stars evolve in a really short time and lose their outer layers due to strong stellar winds really fast. There is a class of stars, the **Wolf-Rayet** or WR stars whose spectra are helium-rich and hydrogen-deficient which are thought to have lost their outer layers revealing directly the by-products of the CNO cycle (original CNO recycled to mostly N -- WN stars) or even the triple alpha (first production of new elements, mainly C -- WC stars). Almost all WR stars are binary stars which may help the envelope stripping process.

30

## The Dredge-ups

H shell burning $\longrightarrow$ He core $\downarrow$, $T \uparrow$

$\Downarrow$

envelope expands $\longrightarrow$ red giant branch (RGB)

$\downarrow$

CNO cycle $\longrightarrow$ low $T$, high opacity, $\nabla T \uparrow$

$\therefore$ convective envelope

$\downarrow$

Material in the core brought up and mixed with envelope

$\Rightarrow$ The (first) dredge-up

Photosphere observed $N \uparrow$ at the expenses of C and O

31

He flash

If $M > 0.5 M_\odot \rightarrow$ He core burning (He "main sequence") (lasting v. short)

He shell burning $\longrightarrow$ asymptotic giant branch (AGB)

$\Rightarrow$ The second dredge-up

$3\alpha$ process $\longrightarrow$ unstable $\rightarrow$ thermal pulses

Heavy elements in spectra of evolved stars $\leftrightarrow$ YSOs $\Rightarrow$ obs. test of stellar evolution

32

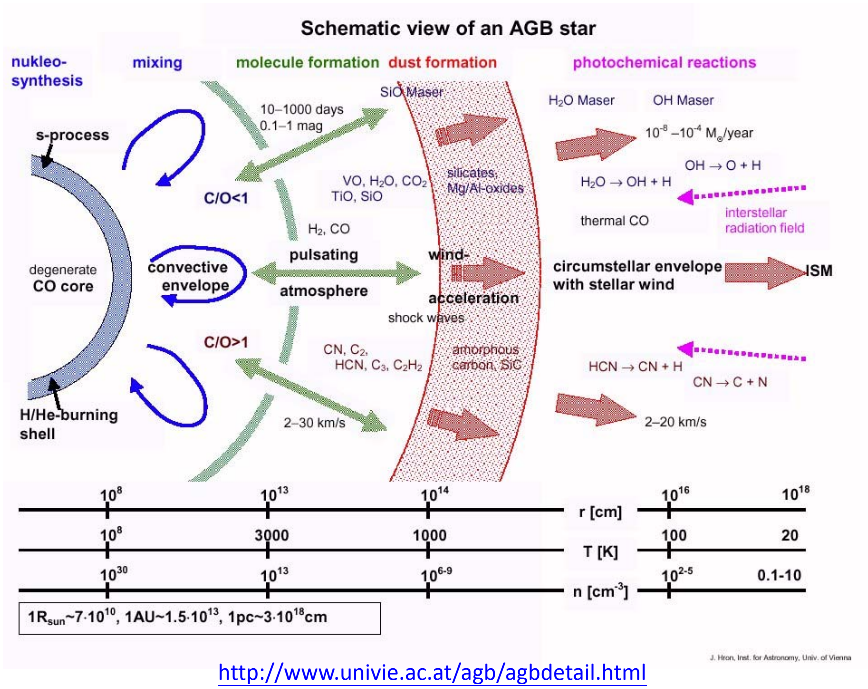


http://www.univie.ac.at/agb/agbdetail.html

33

# Electron Degeneracy

34

<u>**Fermi-Dirac distribution**</u> for non-interacting, indistinguishable particles obeying Pauli exclusion principle; applicable to half-integer spin in TE. Examples of fermions include the electron, proton, neutrons, $^3$He (2 $e^-$, 2 $p^+$, 1 $n^0$)

<u>**Bose-Einstein distribution**</u> for particles not limited to single occupancy of the same energy state. i.e., that do not obey Pauli exclusion principle; with integer values of spin. Example bosons include $^4$He, the Higgs boson, gauge boson, graviton, meson.

35

A Fermi gas is called degenerate if the temperature is low in comparison with the Fermi temperature/energy.

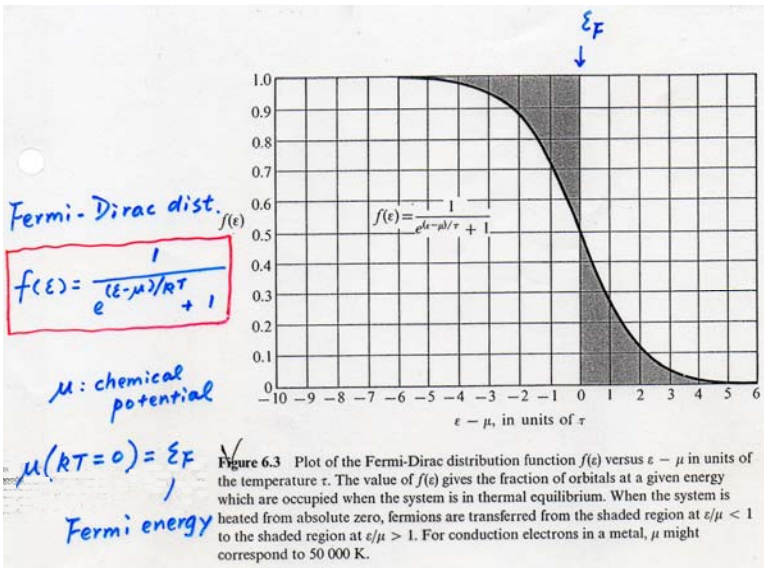


Figure 6.3 Plot of the Fermi-Dirac distribution function $f(\varepsilon)$ versus $\varepsilon - \mu$ in units of the temperature $\tau$. The value of $f(\varepsilon)$ gives the fraction of orbitals at a given energy which are occupied when the system is in thermal equilibrium. When the system is heated from absolute zero, fermions are transferred from the shaded region at $\varepsilon/\mu < 1$ to the shaded region at $\varepsilon/\mu > 1$. For conduction electrons in a metal, $\mu$ might correspond to 50 000 K.

36

## Chemical Potential (μ)

- Temperature governs the flow of energy between two systems.
- Chemical potential governs the flow of particles; from higher chemical potential to the lower



Bose-Einstein dist.

$$\boxed{f(\varepsilon) = \frac{1}{e^{(\varepsilon-\mu)/RT} - 1}}$$

Classical Limit

$$\boxed{f(\varepsilon) \ll 1}$$

$$\boxed{f(\varepsilon) = e^{-(\varepsilon-\mu)/RT}}$$

Maxwell-Boltzmann dist.

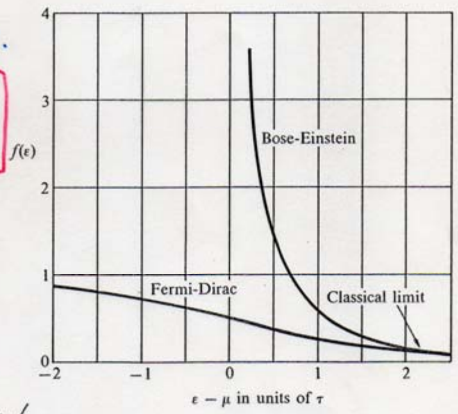


**Figure 6.6** Comparison of Bose-Einstein and Fermi-Dirac distribution functions. The classical regime is attained for $(\varepsilon - \mu) \gg \tau$, where the two distributions become nearly identical. We shall see in Chapter 7 that in the degenerate regime at low temperature the chemical potential $\mu$ for a FD distribution is positive, and changes to negative at high temperature.

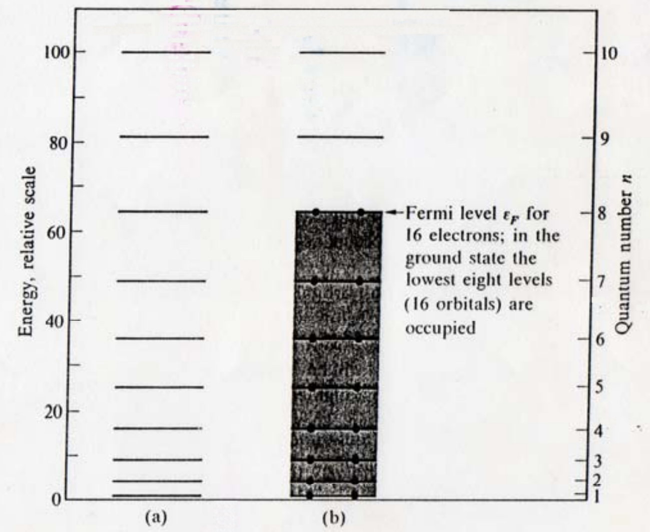


**Figure 7.1** (a) The energies of the orbitals $n = 1, 2, \ldots, 10$ for an electron confined to a line of length $L$. Each level corresponds to two orbitals, one for spin up and one for spin down. (b) The ground state of a system of 16 electrons. Orbitals above the shaded region are vacant in the ground state.

39

As time goes on, electron degeneracy becomes increasingly important,

e.g., $P_e^{deg} \sim 1.7\%$ of total pressure at $\tau \sim 0$

$\sim 7.5\%$ " $\tau \sim 9.2 \times 10^9\,yr$

Taking electron deg. pressure into account,

$M_{isothermal\ core} \sim 0.13\ M_\odot$

$\Rightarrow$ pressure insufficient to support overlying layers

$\Rightarrow$ core contraction $\Rightarrow$ heated, $\epsilon_{nuc} \uparrow$

$\Rightarrow$ Overlying layers pushed outwards

$\Rightarrow$ $\epsilon_{nuc}$ in a narrowing shell

End of main-sequence phase

40

Structural changes during Post-Main Sequence

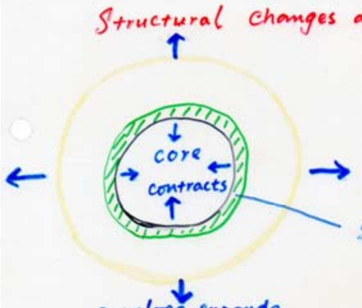


Shell burning, $\epsilon_{shell} \rightarrow L_{shell}$

$\Downarrow$

adds mass to core

$\Downarrow$

core contracts $\Rightarrow T_c \uparrow$

envelope expands

$T_{eff} \downarrow$

$L_* \approx L_{shell}$

$L_{shell}$ heats core $\longrightarrow$ core $\approx$ isothermal

$\therefore$ needs density gradient to support against gravity

41

For low-mass stars ( $0.7 - 2 M_\odot$ )

$\rho_c$ is high $\longrightarrow$ $e^-$ degeneracy sets in before core He burning begins

When He burning starts $\longrightarrow$ $T_c \uparrow$ (but $P_c$ does not)

$\longrightarrow \epsilon \uparrow\uparrow$

$\Rightarrow$ He flash

$E_{release} \sim 10^{11} L_\odot$ in a few seconds

Energy absorbed by envelope (being pushed)

no observable effects !

42

WHY IS THERE A HELIUM FLASH?

normal ideal gas $P\uparrow \Rightarrow T\uparrow$

$\therefore$ Energy input $\Rightarrow T\uparrow \Rightarrow P\uparrow \Rightarrow$ expand

$\Downarrow$

stable against thermal instability $T\downarrow$

$\Rightarrow$ a safty-valve mechanism

If the helium core is degenerate

$P \not\leftrightarrow T$

when $T \gtrsim 10^8$ K, $T\uparrow\uparrow \Rightarrow$ runaway thermal instability

within a few seconds, He ignited

$\Rightarrow$ helium flash

43

The helium flash occurs for $M_{\text{core}} \approx 1\ M_\odot$

If $\mathcal{M} \leq 0.5\ \mathcal{M}_\odot$ $\rightarrow$ core never hot enough

If $\mathcal{M} \geq 2.25\ \mathcal{M}_\odot$ $\rightarrow$ core too hot, He ignited before a degenerate core develops

➔ Only $\mathcal{M} \approx 0.5 - 2.25\ \mathcal{M}_\odot$ stars experience the He flash.

44

After the helium flash

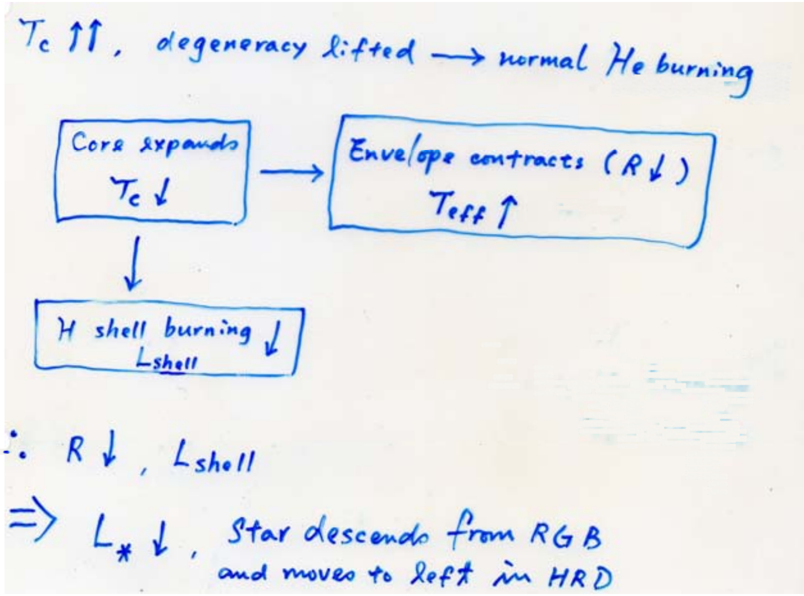


45

Core He burning is much shorter than the MS phase of core H burning, because He is short in abundance, not as efficient in energy supply (1/10 per mass), and the stellar luminosity is higher.

46

HB: L~50-100 $L_\odot$, $\tau \sim 10^8$ yrs

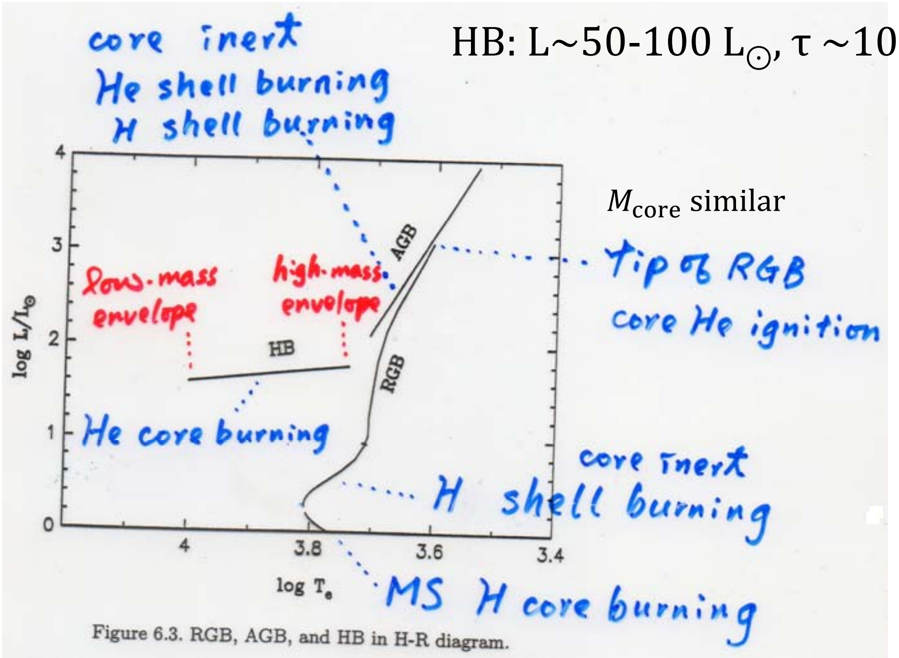


Figure 6.3. RGB, AGB, and HB in H-R diagram.

$M_{core}$ similar

47

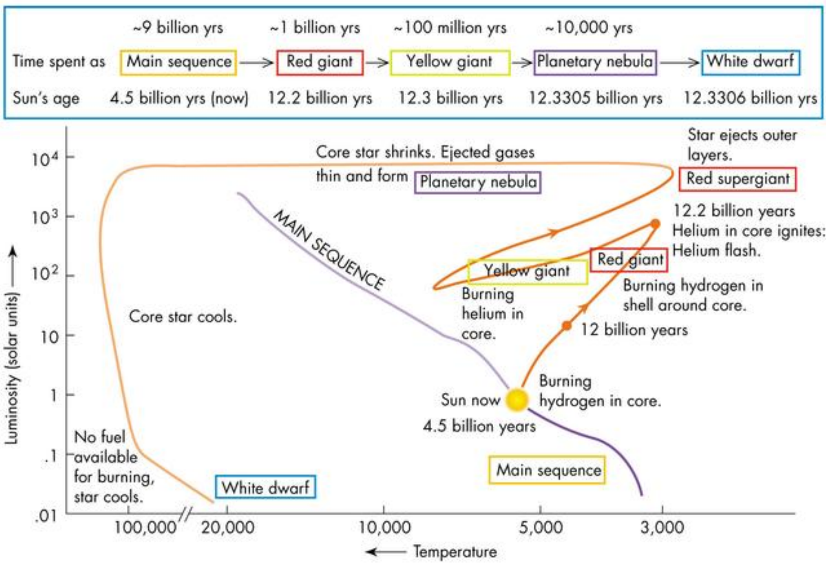


# Evolution of the Sun in the HRD

- MS (core H burning)
- Subgiant branch (shell H burning)
- Red giant branch (shell H burning)
- Red giant (core He flash)
- Horizontal branch (core He burning)
- Asymptotic giant branch (shell He burning)
- Red supergiant
- Protoplanetary nebula
- Planetary nebula
- White/black dwarf

48

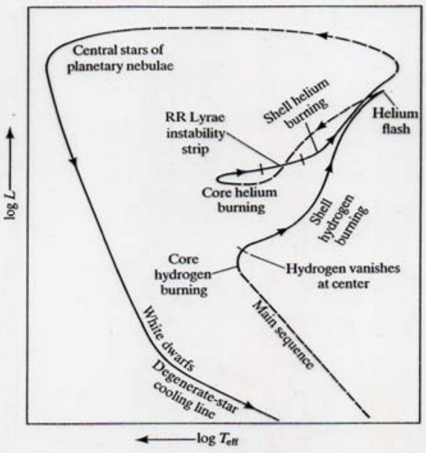


**Figure 3-18.** Schematic evolution track for a representative low-mass, globular-cluster star from the main sequence to its ultimate demise as a white dwarf. The major energy sources are indicated at several key phases. Dashed lines indicate episodes of very rapid evolution, during which details of the structure of the star are, at present, not too well known. Compare this figure with Figure 3-13.

Mihalas & Binney

49

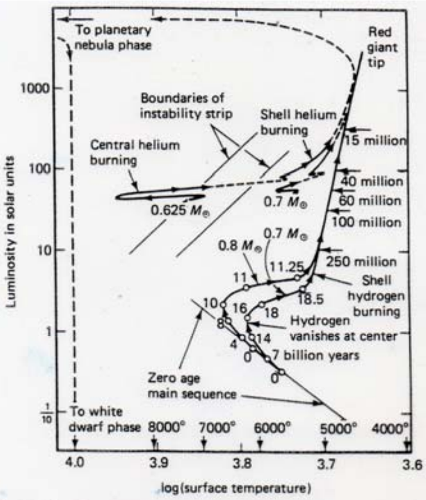


*Fig. 14.11.* Evolutionary tracks for population II stars with 0.7 and 0.8 $M_\odot$. A helium abundance of $Y = 0.30$ and a heavy element abundance of $Z = 10^{-3}$ was used. On the main sequence and subgiant branches evolution times since arrival on the zero age main sequence are given in billions of years. On the red giant branch evolution times from one arrow to the next are given in millions of years. Also indicated is the instability strip, the $T_{eff}$, $L$ domain in which stars start to pulsate (see Chapter 17). From the tip of the asymptotic giant branch the stars probably evolve through the planetary nebula stage to become white dwarfs as indicated by the long dashed lines. From Iben (1971).

50

## The red clump = HB (core He burning) of metal-rich stars

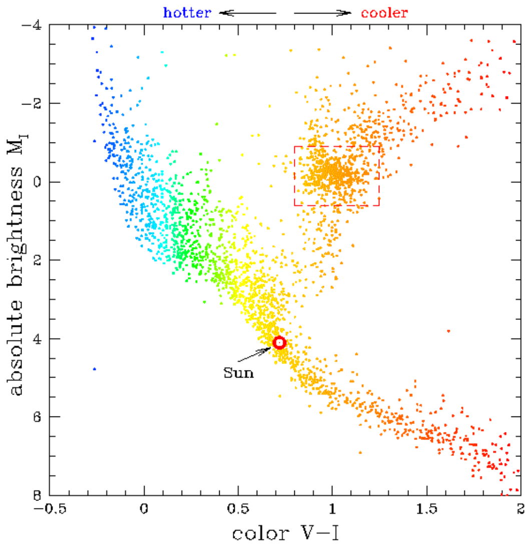


http://www.astronomy.ohio-state.edu/~kstanek/CfA/RedClump/

51

## $L_{RC}$ independent of composition or age ➔ standard candles

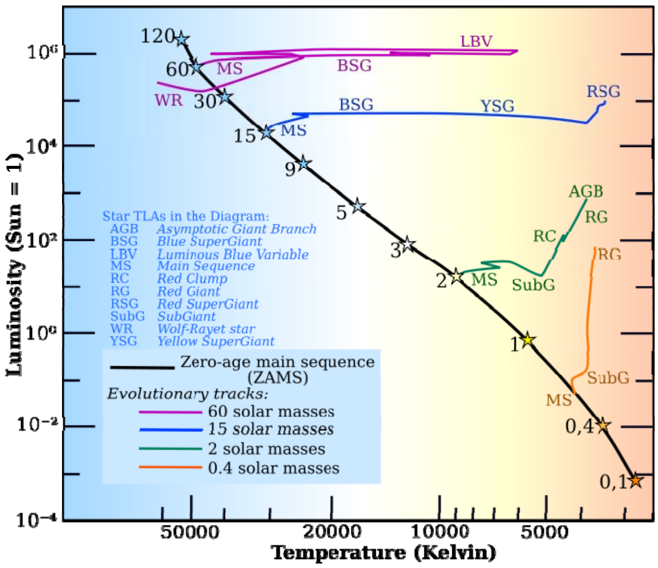


52

Distance to M31 With the *HST* and *Hipparcos* Red Clump Stars (1998)

K. Z. Stanek & P. M. Garnavich

$M_I = -0.23$

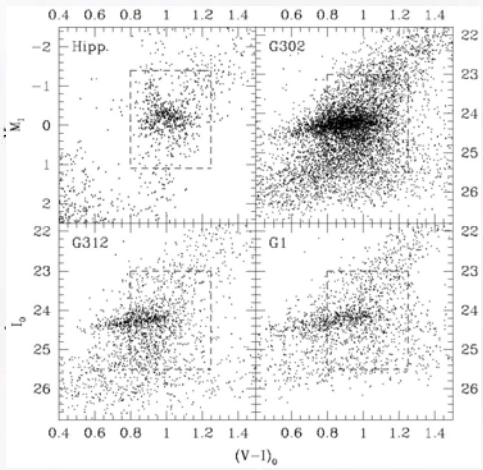


Fig. 2.— The red clump dominated parts of CMDs for the *Hipparcos* stars (upper-left panel) and for three fields in M31 observed with the HST. The dashed rectangles surround the red clump regions used for the comparison between the local and the M31 red clump stars.

Using the red clump stars to determine the distance to M31

Systematic

$$R_{M31} = 784 \pm 13 \pm 17\ kpc$$

Statistical error

53

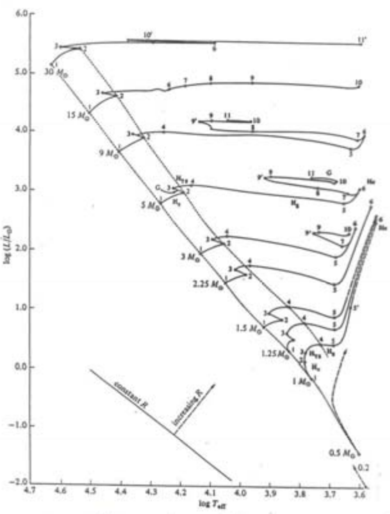


Table 7-7 Evolutionary Times. The times, expressed in years, refer ... tervals between the points in Fig. 7-25.* [Adapted from I. Iben, Jr., 1967 (327).]

| MASS ($M_\odot$) \ INTERVAL | 1–2 | 2–3 | 3–4 | 4–5 | 5–6 |
|---|---|---|---|---|---|
| 30 | 4.80 (6) | 8.64 (4) | ← | ~1.0 (4) | → |
| 15 | 1.010 (7) | 2.270 (5) | ← | 7.55 (4) | → |
| 9 | 2.144 (7) | 6.053 (5) | 9.113 (4) | 1.477 (5) | 6.552 (4) |
| 5 | 6.547 (7) | 2.173 (6) | 1.372 (6) | 7.532 (5) | 4.857 (5) |
| 3 | 2.212 (8) | 1.042 (7) | 1.033 (7) | 4.505 (6) | 4.238 (6) |
| 2.25 | 4.802 (8) | 1.647 (7) | 3.696 (7) | 1.310 (7) | 3.829 (7) |
| 1.5 | 1.553 (9) | 8.10 (7) | 3.490 (8) | 1.049 (8) | ≥2 (8) |
| 1.25 | 2.803 (9) | 1.824 (8) | 1.045 (9) | 1.463 (8) | ≥4 (8) |
| 1.0 | 7 (9) | 2 (9) | 1.20 (9) | 1.57 (8) | ≥1 (9) |

| MASS ($M_\odot$) \ INTERVAL | 6–7 | 7–8 | 8–9 | 9–10[(?)] | 10[(?)]–11[(?)] |
|---|---|---|---|---|---|
| 30 | ← | 53.1 (4) | | → | 1.3 (4) |
| 15 | 7.17 (5) | 6.20 (5) | 1.9 (5) | 3.5 (4) | |
| 9 | 4.90 (5) | 9.50 (4) | 3.28 (6) | 1.55 (5) | 2.86 (4) |
| 5 | 6.05 (6) | 1.02 (6) | 9.00 (6) | 9.30 (5) | 7.69 (4) |
| 3 | 2.51 (7) | 4.08 (7) | | 6.00 (6) | |

* A number in parentheses is the power of 10 by which an entry is to be multiplied.

*Fig. 7-25* Evolutionary Tracks in the Hertzsprung–Russell Diagram. The mass of each star is given at the left of the track. The composition is $X = 0.708$, $Y = 0.272$, and $Z = 0.020$ for all masses except 30 $M_\odot$, for which the composition is $X = 0.70$, $Y = 0.27$, $Z = 0.03$. *Dashed portions* of the curves are estimates. The *letters* along the tracks for 1 $M_\odot$ and 5 $M_\odot$ have the following significance: $H_c$ = hydrogen-burning near the center; $G$ = gravitational contraction of the entire star; $H_{TS}$ = hydrogen-burning in a thick shell; $H_s$ = hydrogen-burning in a thin shell; He = helium-burning near the center plus hydrogen-burning in a thin shell. The times required to reach the encircled points are given in Table 7-7.

The *dotted lines* indicate the boundaries of the main sequence. The *line* (*lower left*) shows the slope of a path along which the radius remains constant. The track for 15 $M_\odot$ does not turn back as do the other tracks because the semi-convective zone was treated as fully convective [see R. Stothers and C.-W. Chin, 1968 (377)]. [Adapted from I. Iben, Jr., 1967 (327). The track for 30 $M_\odot$ is given by R. Stothers, 1966 (333).]

$H_c$ : H core burning
$H_{TS}$ : H thick shell
$T_s$ : H thin shell

54

For high-mass stars, e.g., $5\,M_\odot$

③

$L_{grav}$ contributes ; $L_r \uparrow$ for $M_r < 0.1\,M$

$\Rightarrow \nabla T \Rightarrow$ later He burning begins before $e^-$ deg. sets in

Shell burning pushes the core and envelope → $L_r\,(r > 0.2)\downarrow$

$\epsilon_{shell} \uparrow\uparrow \Rightarrow$ envelope expands $\uparrow\uparrow$

↳ adds mass until Schönberg-Chandrasekhar limit ④

$\Rightarrow$ core contracts, $T_c \uparrow \longrightarrow \epsilon_{shell} \uparrow\uparrow\uparrow$

pushes envelope, $T_{eff} \downarrow$, $L_r \lesssim$ const

55

End of core contraction

③

*Fig. 7-28A* A Model of Mass $5\,M_\odot$ Shortly after Leaving the Main Sequence, at $t = 6.82461 \times 10^7$ Years. Radius $r$, pressure $P$, density $\rho$, temperature $T$, net luminosity $L_r$, and hydrogen abundance $X$ are shown as functions of fractional mass $M_r/M$. The lower limit of the ordinate is zero for all variables. The upper limits, given in the figure, are $2.9198\,R_\odot$ (with $R_\odot = 6.96 \times 10^{10}$ cm; however, the total radius is $3.9429\,R_\odot$), central pressure $P_c$ (dyne cm$^{-2}$), central density $\rho_c$ (gm cm$^{-3}$), central temperature $T_c$ (°K), total luminosity $L$ (units of $L_\odot = 3.86 \times 10^{33}$ erg sec$^{-1}$), and initial hydrogen abundance $X = 0.708$. The time is measured from the initial model calculated for the pre-main-sequence phase. [Adapted from I. Iben, Jr., 1966 (331).]

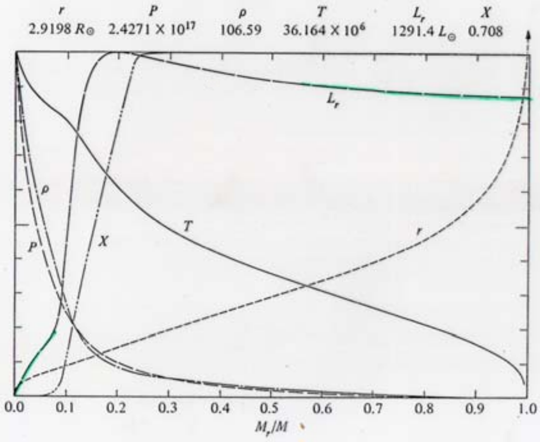


56

$\tau_{④-⑤} \sim 7.5 \times 10^5$ yr (i.e., v. short)

→ Hertzsprung gap

$\tau_{⑤-⑥} \sim 5 \times 10^5$ yr

⑥ = tip of RGB
= onset of He burning
$T_c \sim 2 \times 10^8$ K

But core is nondegenerate

∴ core expands, $\epsilon_{core} \downarrow$

↓

envelope contracts, $T_{eff} \uparrow$

57

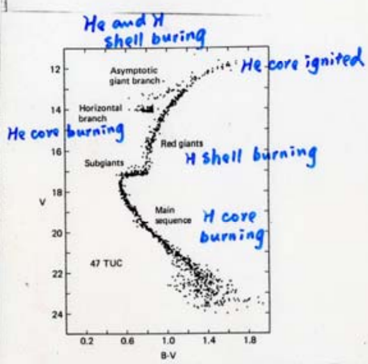


*Fig. 1.7.* The color apparent magnitude diagram for 47 Tucanae. The new measurements go down to stars as faint as 23rd magnitude, though for the faint stars the scatter becomes large. The main sequence and the giant and subgiant branches are surprisingly sharp, showing that there are very few or no binaries in this globular cluster. The red stub of the horizontal branch is seen at V ~ 14 and B − V ~ 0.8. The asymptotic giant branch (see Chapter 14) is seen above the horizontal branch. From Hesser *et al.* (1987).

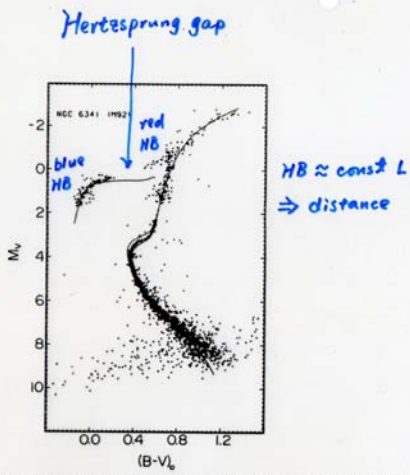


*Fig. 1.8.* The color absolute magnitude diagram for the globular cluster M92 (cluster 92 in the Messier catalog of nebulous objects). The new observations for M92, like those for 47 Tuc, go to very faint magnitudes. For M92 the main sequence is now clearly recog-izable. In addition the subgiant, red giant and horizontal branches are clearly seen. Also seen is the so-called asymptotic branch, for $(B - V)_0 \sim 0.6$ above the horizontal branch. The thin lines shown are the theoretical isochrones, i.e. the location where stars are expected to be seen at a given time. From Hesser *et al.* (1987).

HB morphology differs from one GC to another.

58

After ⑤

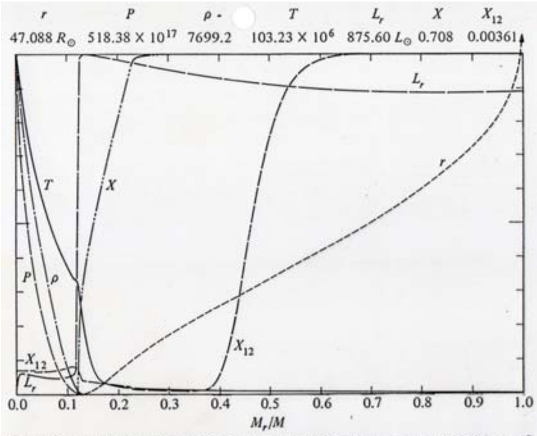


*Fig. 7-28B* A Model of Mass 5 $M_\odot$ during the Giant Stage at $t = 7.03776 \times 10^7$ Years. Radius $r$, pressure $P$, density $\rho$, temperature $T$, net luminosity $L_r$, hydrogen abundance $X$, and carbon-12 abundance $X_{12}$ are shown as functions of fractional mass $M_r/M$. The lower limit of the ordinate is zero for all variables. The upper limits, given in the figure, are 47.088 $R_\odot$ (with $R_\odot = 6.96 \times 10^{10}$ cm; however, the total radius is 51.328 $R_\odot$), central pressure $P_c$ (dyne cm$^{-2}$), central density $\rho_c$ (gm cm$^{-3}$), central temperature $T_c$ (°K), total luminosity $L$ (units of $L_\odot = 3.86 \times 10^{33}$ erg sec$^{-1}$), initial hydrogen abundance $X = 0.708$, and carbon-12 abundance $X_{12} = 0.003610$. The time is measured from the initial model calculated for the pre-main-sequence phase. [Adapted from I. Iben, Jr., 1966 (331).]

At the center, $N^{14}(\alpha,\gamma)F^{18}(\beta^+,\nu)O^{18}$

59

5 $M_\odot$ (continued)

From ⑥ → ⑦

$\epsilon_{core} \downarrow \rightarrow L_* \downarrow$

$T_{eff} \uparrow$

But as $T_{envelope} \uparrow \rightarrow$ opacity $\downarrow \Rightarrow L_* \uparrow$

60

Between points ⑦ and ⑧

*Fig. 7-28C* A Model of Mass 5 $M_\odot$ during the Giant Stage at $t = 7.73665 \times 10^7$ Years. Radius $r$, pressure $P$, density $\rho$, temperature $T$, net luminosity $L_r$, and helium-4 abundance $X_4$ are shown as functions of fractional mass $M_r/M$. The lower limit of the ordinate is zero for all variables. The upper limits, given in the figure, are 35.852 $R_\odot$ (with $R_\odot = 6.96 \times 10^{10}$ cm; however, the total radius is 50.612 $R_\odot$), central pressure $P_c$ (dyne cm$^{-2}$), central density $\rho_c$ (gm cm$^{-3}$), central temperature $T_c$ (°K), total luminosity $L$ (units of $L_\odot = 3.86 \times 10^{33}$ erg sec$^{-1}$), and helium-4 abundance $X_4 = 0.9763$. The time is measured from the initial model calculated for the pre-main-sequence phase (see Section 2). [Adapted from I. Iben, Jr., 1966 (331).]

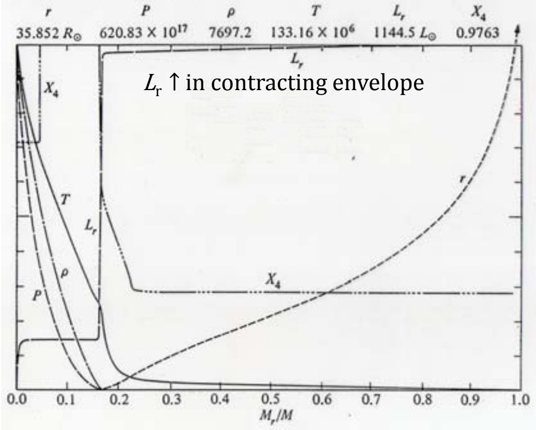


61

Point 11 Two shells at $M_r$=0.07 (He) and 0.22 (H)

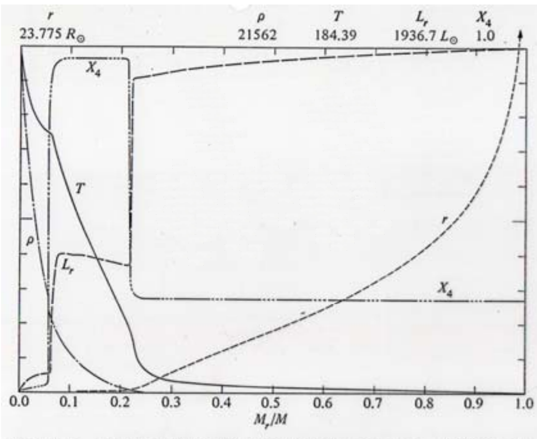


*Fig. 7-28D* A Model of Mass 5 $M_\odot$ during the Giant Stage at $t = 8.79060 \times 10^7$ Years. Radius $r$, density $\rho$, temperature $T$, net luminosity $L_r$, and helium-4 abundance $X_4$ are shown as functions of fractional mass $M_r/M$. The lower limit of the ordinate is zero for all variables. The upper limits, given in the figure, are 23.775 $R_\odot$ (with $R_\odot = 6.96 \times 10^{10}$ cm; however, the total radius is 44.141 $R_\odot$), central density $\rho_c$ (gm cm$^{-3}$), central temperature $T_c$ (°K), total luminosity $L$ (units of $L_\odot = 3.86 \times 10^{33}$ erg sec$^{-1}$), and helium-4 abundance $X_4 = 1.0$. The time is measured from the initial model calculated for the pre-main-sequence phase. [Adapted from I. Iben, Jr., 1966 (331).]

62

MS Stars

AGB

wind → envelope

WD

$M = 1\text{-}9\,M_\odot$ ⟶ C-O core $0.6\text{-}1.1\,M_\odot$

roughly core mass ↔ MS mass

⇒ expect WD mostly $0.6\,M_\odot$

During AGB, H-shell and He-shell burning

bottom of He layer

Envelope shed = a random process in pulses

63

If H-shell burning → WD w/ a thin layer of H

80% of all DA white dwarfs

(H lines, no He lines nor metal lines)

If He-shell burning → WD He layer

less freq.

DB (He I lines, no H, metals)

16%

⇒ expect more DA white dwarfs than DBs

obs 25% He lines

DC (continuous, no lines)

DO (He II lines)

*DQ (C dominated)*

64

- Origins of DA and non-DA uncertain: (1) exact phase when the last thermal pulse takes place after the AGB phase, or (2) convective mixing, radiative levitation, or diffusion.

$M = 0.7 - 1.0 M_\odot$

MS → RG – He core $\lesssim 0.4 M_\odot$ WD

no AGB, PN phases

65

A&A 419, L5–L8 (2004)

## Mass distribution of DA white dwarfs in the First Data Release of the Sloan Digital Sky Survey

J. Madej[1], M. Należyty[1], and L. G. Althaus[2]

[1] Astronomical Observatory, University of Warsaw, Al. Ujazdowskie 4, 00-478 Warsaw, Poland
[2] Departament de Fisica Aplicada, Universitat Politecnica de Catalunya, Av. del Canal Olimpic s/n, 08860, Castelldefels, Spain

Received 4 March 2004 / Accepted 23 March 2004

**Abstract.** We investigate the sample of 1175 new nonmagnetic DA white dwarfs with the effective temperatures $T_{\rm eff} \geq$ 12 000 K, which were extracted from the Data Release 1 of the Sloan Digital Sky Survey. We determined masses, radii, and bolometric luminosities of stars in the sample. The above parameters were derived from the effective temperatures $T_{\rm eff}$ and surface gravities $\log g$ published in the DR1, and the new theoretical $M-R$ relations for carbon-core and oxygen-core white dwarfs. Mass distribution of white dwarfs in this sample exhibits the peak at $M = 0.562\ M_\odot$ (carbon-core stars), and the tail towards higher masses. Both the shape of the mass distribution function and the empirical mass-radius relation are practically identical for white dwarfs with either pure carbon or pure oxygen cores.

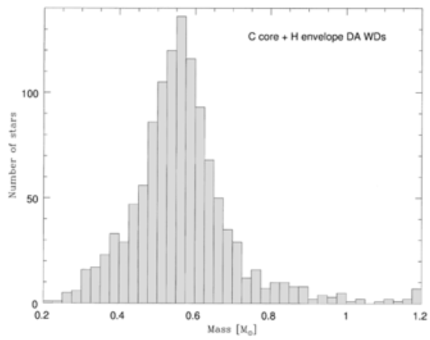


66

## $\mathcal{M} < 0.7\ M_\odot$

$< 0.16\ M_\odot \rightarrow$ no RGB

$< 0.5\ M_\odot \rightarrow \tau_{MS} > \tau_{Universe}$

$< 0.5 \sim 0.7\ M_\odot \rightarrow$ no core He burning

Very low-mass stars are completely convective
$\rightarrow$ more H to burn $\rightarrow \tau_{MS}$ lengthened

67

## A 1 $M_\odot$ main sequence star

- $\tau_{MS} \sim 10^{10}$ yrs
- $\tau_{RGB} \sim 10^{9}$ yrs
- $\tau_{HB} \sim 10^{8}$ yrs
- $\tau_{AGB} \sim 2 \times 10^{7}$ yrs
- $\tau_{PS} \sim 5 \times 10^{4}$ yrs

A remnant of a 0.6 WD

68

## $\mathcal{M} < 25\ \mathrm{M}_\odot$

Mass loss rate low

$\boldsymbol{\mathcal{M} = 20} - 25\ \mathrm{M}_\odot$
O type star → red supergiant → supernova

$\boldsymbol{\mathcal{M} < 20}$
O type star → red supergiant → Cepheid
→ red supergiant → supernova

69

## $\mathcal{M} = 25 - 60\ \mathrm{M}_\odot$

Mass loss not sufficient to remove the entire envelope

$\boldsymbol{\mathcal{M} = 40} - 60\ \mathrm{M}_\odot$
O type star → blue super giant → yellow supergiant
→ red supergiant
→ blue supergiant → WN → supernova

$\boldsymbol{\mathcal{M} = 25} - 40\ \mathrm{M}_\odot$
O type star → blue super giant → yellow supergiant
→ red supergiant
→ supernova

70

## $\mathcal{M} > 60\ M_\odot$

Mass loss fierce $\approx 10^{-1}\ M_\odot\ yr^{-1}$, rid of almost entire envelope during the LBV stage, left with a WR star, evolving toward a SN.

O type star → Of star → blue super giant

→ luminous blue variable → WN star
→ WC star → supernova

71

A&A 564, A30 (2014)

**The evolution of massive stars and their spectra**

**I. A non-rotating 60 $M_\odot$ star from the zero-age main sequence to the pre-supernova stage★,★★**

Jose H. Groh[1], Georges Meynet[1], Sylvia Ekström[1], and Cyril Georgy[2]

[1] Geneva Observatory, Geneva University, Chemin des Maillettes 51, 1290 Sauverny, Switzerland
e-mail: jose.groh@unige.ch
[2] Astrophysics group, EPSAM, Keele University, Lennard-Jones Labs, Keele, ST5 5BG, UK

**ABSTRACT**

For the first time, the interior and spectroscopic evolution of a massive star is analyzed from the zero-age main sequence (ZAMS) to the pre-supernova (SN) stage. For this purpose, we combined stellar evolution models using the Geneva code and stellar atmospheric/wind models using CMFGEN. With our approach, we were able to produce observables, such as a synthetic high-resolution spectrum and photometry, thereby aiding the comparison between evolution models and observed data. Here we analyze the evolution of a non-rotating 60 $M_\odot$ star and its spectrum throughout its lifetime. Interestingly, the star has a supergiant appearance (luminosity class I) even at the ZAMS. We find the following evolutionary sequence of spectral types: O3 I (at the ZAMS), O4 I (middle of the H-core burning phase), B supergiant (BSG), B hypergiant (BHG), hot luminous blue variable (LBV; end of H-core burning), cool LBV (H-shell burning through the beginning of the He-core burning phase), rapid evolution through late WN and early WN, early WC (middle of He-core burning), and WO (end of He-core burning until core collapse). We find the following spectroscopic phase lifetimes: $3.22 \times 10^6$ yr for the O-type, $0.34 \times 10^5$ yr (BSG), $0.79 \times 10^5$ yr (BHG), $2.35 \times 10^5$ yr (LBV), $1.05 \times 10^5$ yr (WN), $2.57 \times 10^5$ yr (WC), and $3.80 \times 10^4$ yr (WO). Compared to previous studies, we find a much longer (shorter) duration for the early WN (late WN) phase, as well as a long-lived LBV phase. We show that LBVs arise naturally in single-star evolution models at the end of the MS when the mass-loss rate increases as a consequence of crossing the bistability limit. We discuss the evolution of the spectra, magnitudes, colors, and ionizing flux across the star's lifetime, and the way they are related to the evolution of the interior. We find that the absolute magnitude of the star typically changes by ~6 mag in optical filters across the evolution, with the star becoming significantly fainter in optical filters at the end of the evolution, when it becomes a WO just a few $10^4$ years before the SN explosion. We also discuss the origin of the different spectroscopic phases (i.e., O-type, LBV, WR) and how they are related to evolutionary phases (H-core burning, H-shell burning, He-core burning).

Read the first 4 paragraphs of this paper.

72

# Stellar Rotation



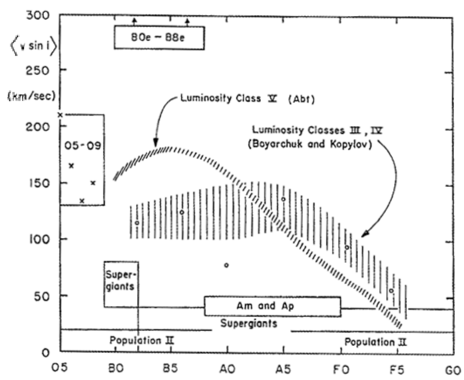


**Fig. 3.** Projected equatorial velocities, averaged over all possible inclinations, as a function of spectral type. On the main sequence (luminosity class V), early-type stars have rotational velocities that reach and even exceed 200 km/s; these velocities drop to a few km/s for late-type stars, such as the Sun (type G2) (Slettebak [20]; courtesy Gordon & Breach)

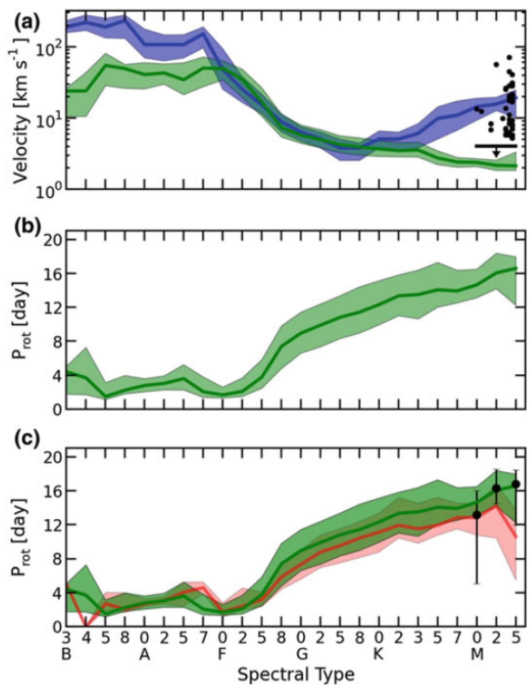


**Fig. 2.2** *Panel A* The *blue curve* is the median equatorial velocity $(4/\pi)\langle v \sin i\rangle$ for each spectral type from Glebocki and Gnacinski (2005). The *green curve* shows the equatorial velocity of the *Kepler* targets, $\bar{v}$(s.t.), derived from the measured rotation periods and the KIC radii. The *black points* show measurements by Reiners and Mohanty (2012). In this sample 201 stars have an upper $v \sin i$ limit of 4 km/s (due to instrumental limitations), these stars are represented by the *solid bar*. *Panel B* The rotation periods $P_{rot}$ of the stars in our sample, averaged within each spectral type. *Panel C* The same as panel B, but for comparison we show the median of the rotation periods measured by McQuillan et al. (2013) (*black points* with *errorbars*), for the stars overlapping with our sample. Similarly, the *red curve* shows the median of the rotation periods found by Debosscher et al. (2011). *Shaded areas* and *error bars* span the *upper* and *lower* 34th percentile values from the median. Reproduced with permission from Astronomy & Astrophysics, © ESO

# Rotation → star cooler and fainter

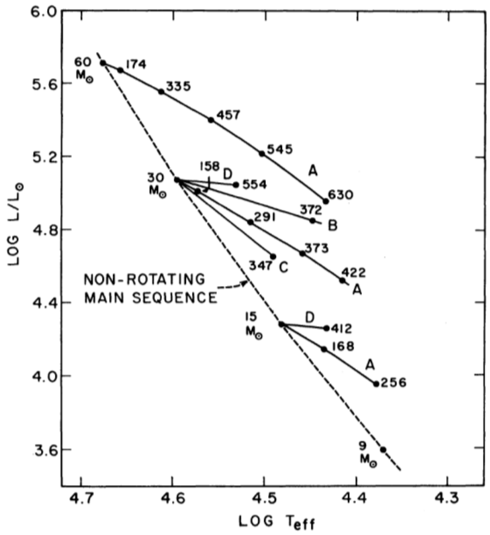


Fig. 2.—Theoretical H-R diagram showing model sequences of increasing angular momentum (*solid curves*). Numbers on curves give calculated velocities at the equator in km sec$^{-1}$. The distribution of angular momentum for each sequence is indicated by the letter A, B, C, or D.

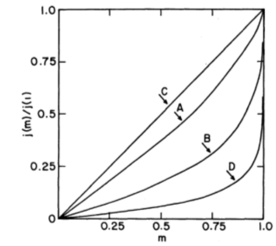


Fig. 1.—Angular momentum per unit mass, as a function of mass fraction interior to a given cylinder about the axis of rotation, for three assumed laws of differential rotation (Cases A, B, and C) and for a uniformly rotating model (Case D) of 30 $\mathfrak{M}_\odot$, log $J$ = 52.73.

$D$: solid body rotation

Rotation law:
angular momentum distribution $j(m_\varpi)$ as a function of, $m_\varpi$, the mass fraction interior to the cylinder of radius $\varpi$ about the rotation axis.

Bodenheimer (1971) ApJ, **167**, 153

## 1. Introduction

Massive stars are essential constituents of stellar populations and galaxies in the near and far Universe. They are among the most important sources of ionizing photons, energy, and some chemical species, which are ejected into the interstellar medium through powerful stellar winds and during their extraordinary deaths as supernovae (SN) and long gamma-ray bursts (GRB). For these reasons, massive stars are often depicted as cosmic engines, because they are directly or indirectly related to most of the major areas of astrophysical research.

Despite their importance, our current understanding of massive stars is still limited. This inconvenient shortcoming can be explained by many reasons on which we elaborate below. First, the physics of star formation mean that massive stars are rare (Salpeter 1955). Moreover, their lifetime is short, of a few to tens of millions of years (e.g., Ekström et al. 2012; Langer 2012). These factors make it challenging to construct evolutionary sequences and relate different classes of massive stars. This is in sharp contrast to what can be done for low-mass stars.

Second, one can also argue that the evolution of massive stars is extremely sensitive to the effects of some physical processes, such as mass loss and rotation (Maeder & Meynet 2000; Heger et al. 2000), that have relatively less impact on the evolution of low-mass stars. However, the current implementation of rotation in one-dimensional codes relies on parametrized formulas, and the choice of the diffusion coefficients has a key impact on the evolution (Meynet et al. 2013). Likewise, mass-loss recipes arising from first principles are only available for main sequence (MS) objects (Vink et al. 2000, 2001) and a restricted range of Wolf-Rayet (WR) star parameters (Gräfener & Hamann 2008). Third, binarity seems to affect the evolution of massive stars, given that a large portion of them are in binary systems that will interact during the evolution (Sana et al. 2012).

Fourth, our understanding of different classes of stars is often built by comparing evolutionary models and observations. However, mass loss may affect the spectra, magnitudes, and colors of massive stars, thus making the comparison between evolutionary models and observations a challenge. In addition to luminosity, effective temperature, and surface gravity, the

76

observables of massive stars can be strongly influenced by a radiatively driven stellar wind that is characteristic of these stars. The effects of mass loss on the observables depend on the initial mass and metallicity, since they are in general more noticeable in MS stars with large initial masses, during the post-MS phase, and at high metallicities. When the wind density is significant, the mass-loss rate, wind clumping, wind terminal velocity, and velocity law have a strong impact on the spectral morphology. This makes the analysis of a fraction of massive stars a difficult task, and obtaining their fundamental parameters, such as luminosity and effective temperature, is subject to the uncertainties that comes from our limited understanding of mass loss and clumping. Furthermore, the definition of effective temperature of massive stars with dense winds is problematic and, while referring to an optical depth surface, it does not relate to a hydrostatic surface. This is caused by the atmosphere becoming extended, with the extension being larger the stronger the wind is. Stellar evolution models are able to predict the stellar parameters only up to the stellar hydrostatic surface, which is not directly reached by the observations of massive stars when a dense stellar wind is present. Since current evolutionary models do not thoroughly simulate the physical mechanisms happening at the atmosphere and wind, model predictions of the evolution of massive stars are difficult to be directly compared to observed quantities, such as a spectrum or a photometric measurement.



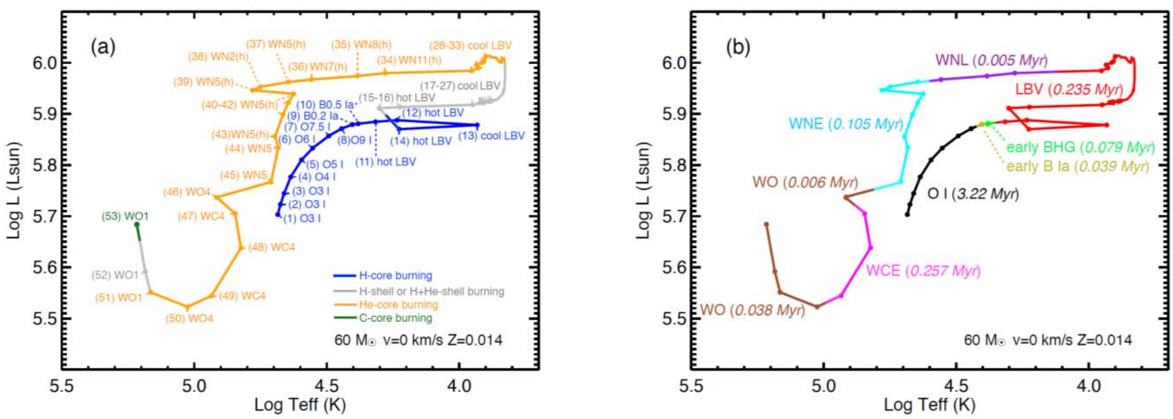


**Fig. 3.** **a)** HR diagram showing the evolutionary track of a non-rotating star with initial mass of 60 $M_\odot$ at metallicity $Z = 0.014$, using our revised values of $T_{\rm eff}$. The color code corresponds to the evolutionary phases of a massive star, with H-core burning in blue, He-core burning in orange, C-core burning in green, and H and/or He-shell burning in gray. **b)** Similar to **a)**, but color coded according to the spectroscopic phases. Lifetimes of each phase are indicated in parenthesis. **c)** Evolution of $T_{\rm eff}$ as a function of age. The color code is the same as in **a)**. **d)** Surface abundances

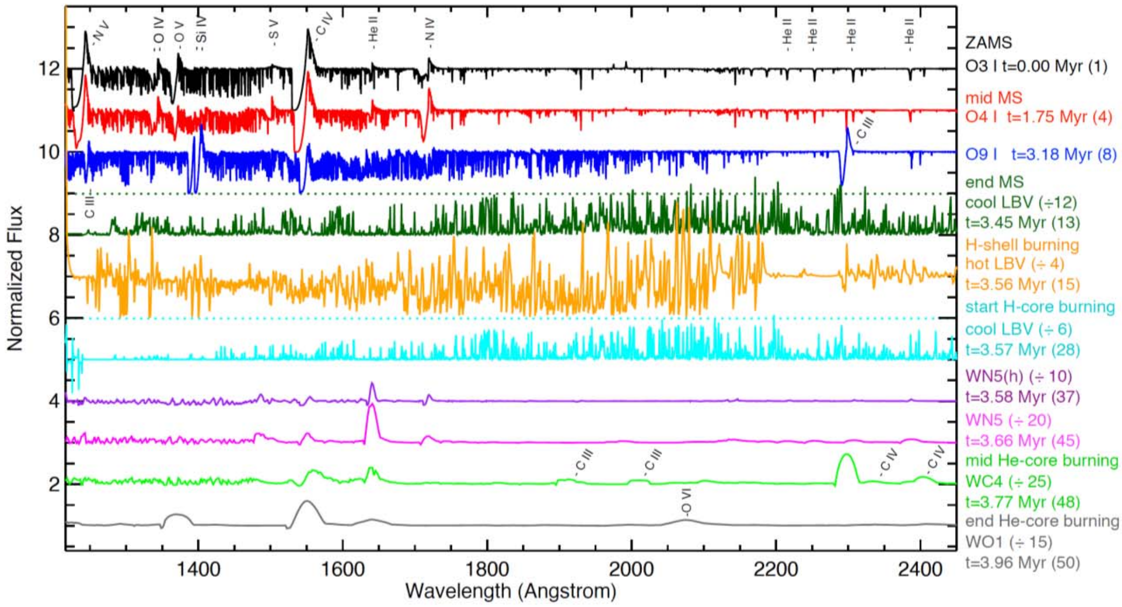


79

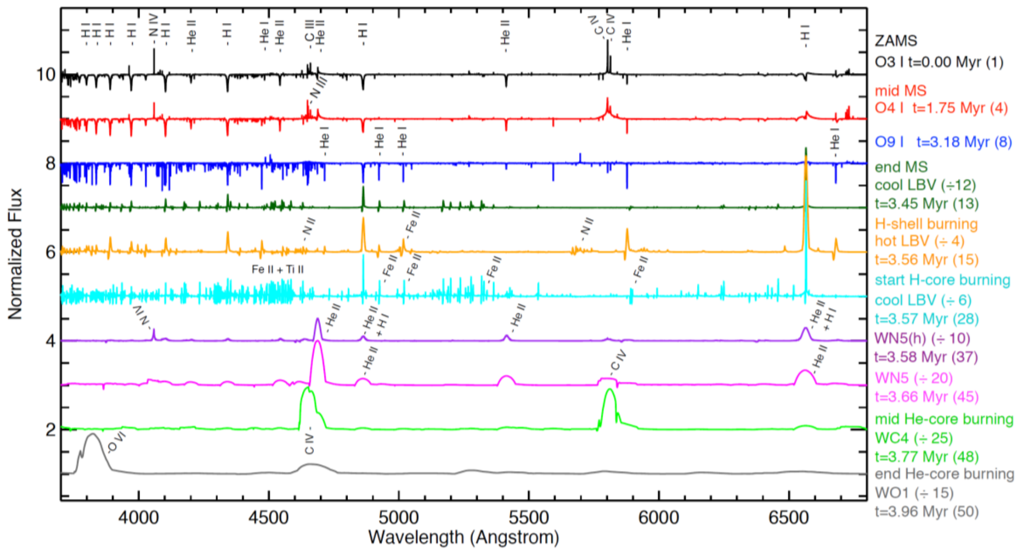


**Fig. 4.** Evolution of the ultraviolet **a)** (*top*) and optical spectra **b)** (*bottom*) of a non-rotating 60 $M_{\odot}$ star. The evolution proceeds from top to bottom, with labels indicating the evolutionary phase, spectral type, scale factor when appropriate, age, and model stage according to Table 1. Note that certain spectra have been scaled for the sake of displaying the full range of UV and optical emission lines.

80

# Test of Stellar Evolution by Star Clusters

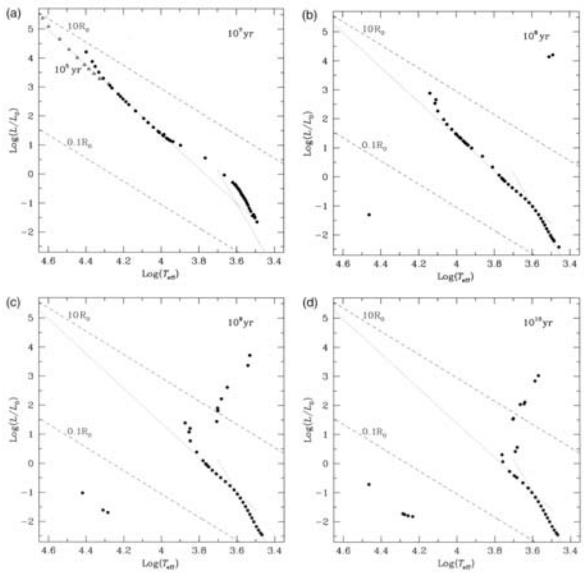


**Figure 9.21** Evolutionary calculations for stars of different masses forming a hypothetical cluster result in an evolving H–R diagram, shown at four ages. The number of stars and their mass distribution is arbitrary. The dashed lines are lines of constant radius. The dotted lines mark the main-sequence slopes. We note that at $10^7$ years (a), the low-mass stars are not yet settled on the main sequence, while the very massive ones have already left it: the open triangles show the main sequence of massive stars at a much earlier epoch, $10^5$ years. The Hertzsprung gap is conspicuous at $10^8$ years (b) resembling the Hyades-cluster H–R diagram shown in Figure 1.5. By contrast, the continuously-populated track toward the red giant branch is clearly seen at later epochs (c and d), when low-mass stars leave the main sequence.

Prialnik

81

82

## Initial Mass Function

The birthrate function $B(M,t)$ is the number of stars per unit volume, with masses between $M$ and $M+dM$ that are formed out of ISM during time interval $t$ and $t+dt$.

$$B(M,t)\,dM\,dt = \psi(t)\,\xi(M)\,dM\,dt,$$

where $\psi(t)$ is the **star formation rate** (SFR),
and $\xi(M)$ is the **initial mass function** (IMF).

For the Galactic disk, SFR is $5.0 \pm 0.5\ M_\odot \mathrm{pc}^{-2}\ \mathrm{Gyr}^{-1}$ integrated over the $z$ direction.

IMF: many more low-mass stars than higher mass stars as a result of cloud fragmentation?

83

The IMF specifies the fractional distribution in mass of a newly formed stellar system. It is often assumed to have a simple power law $\xi(M) = c\,M^{-\alpha} = c\,M^{-(1+\Gamma)}$

In general, $\xi(M)$ extends from a lower to an upper cutoff, e.g., from 0.1 to 125 solar masses. Commonly used IMFs are those of Salpeter (1955), Scalo (1986), and Miller and Scalo (1979).

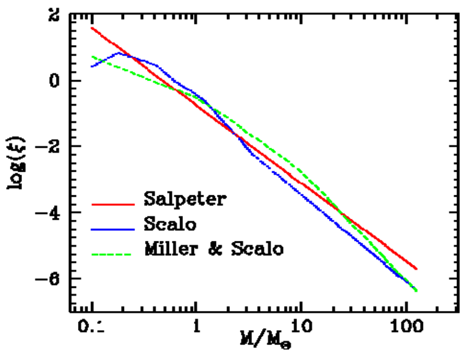


http://webast.ast.obs-mip.fr/hyperz/hyperz_manual1/node7.html

- Edwin Salpeter (1955) on solar-neighborhood stars (ApJ, 121, 161)
  Present-day LF → mass-luminosity relation → present-day mass function → stellar evolution → initial mass function
  $\alpha=2.35$ or $\Gamma = 1.35$
- Glenn E. Miller and John M. Scalo extended work below 1 $M_\odot$
  (1979, ApJS, 41, 513) $\alpha \approx 0$ for $M < 1\ M_\odot$
- Pavel Kroupa (2002, Sci, 295, 82)
  $\alpha = 2.3$ for $M > 0.5\ M_\odot$
  $\alpha = 1.3$ for $0.08\ M_\odot < M < 0.5\ M_\odot$
  $\alpha = 0.3$ for $M < 0.08\ M_\odot$
- A universal IMF among stellar systems (SFRs, star clusters, galaxies) (Bastian et al. 2010, ARAA). But why?

85



# THE LUMINOSITY FUNCTION AND STELLAR EVOLUTION

EDWIN E. SALPETER*
Australian National University, Canberra, and Cornell University
*Received July 29, 1954*

ABSTRACT

The evolutionary significance of the observed luminosity function for main-sequence stars in the solar neighborhood is discussed. The hypothesis is made that stars move off the main sequence after burning about 10 per cent of their hydrogen mass and that stars have been created at a uniform rate in the solar neighborhood for the last five billion years.

Using this hypothesis and the observed luminosity function, the rate of star creation as a function of stellar mass is calculated. The total number and mass of stars which have moved off the main sequence is found to be comparable with the total number of white dwarfs and with the total mass of all fainter main-sequence stars, respectively.

86

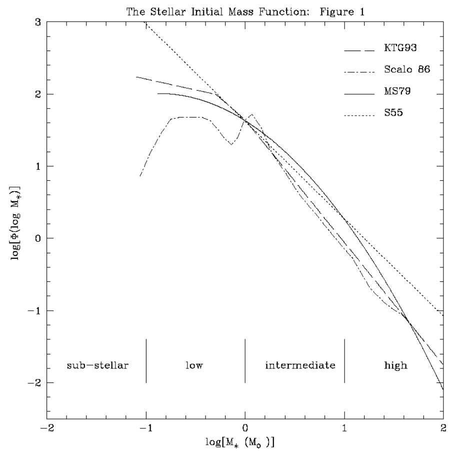


Figure 1. Initial mass function for field stars in the solar neighborhood taken from a variety of recent studies. These results have been normalized at 1 M⊙. For both the MS79 and Scalo 86 IMFs we have adopted 15 Gyr as the age of the Milky Way. Current work suggests that the upper end of the IMF (> 5M⊙) is best represented by a power–law similar to Salpeter (1955) while the low mass end (< 1M⊙) is flatter (Kroupa, Tout, and Gilmore 1993). The shape of the IMF from 1–5 M⊙ is highly uncertain.

From Meyer et al. (2000) Protostars & Planets IV

87

## Orion Nebula Cluster

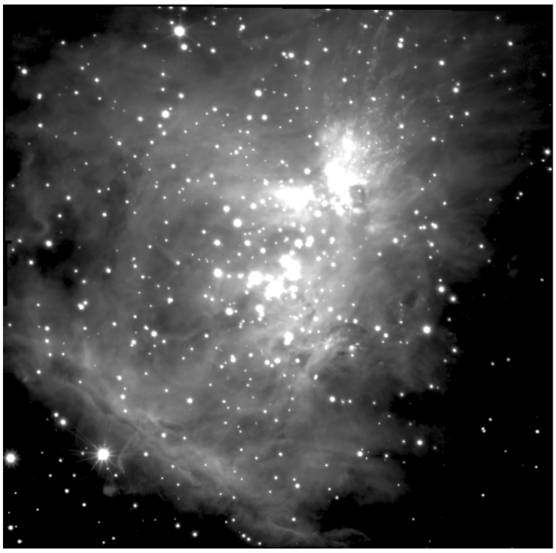

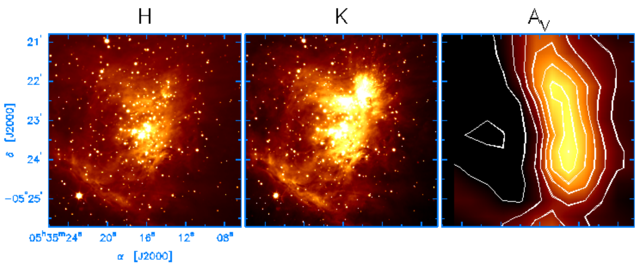


http://www.astro.caltech.edu/~jmc/papers/onc/gif/figure1.gif

88

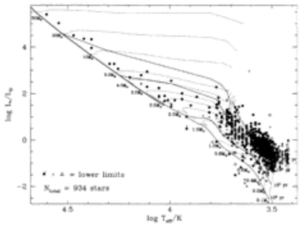


FIG. 12. *HR diagram for the Orion Nebula Cluster.* Triangles indicate lower limits in luminosity. Filled circles/triangles indicate proper motion cluster members plus all sources which have been identified as being externally ionized; open circles/triangles indicate that no proper motion information is available; crosses indicate proper motion nonmembers. Typical errors are ≲0.02 in log $T_{eff}$ for late-type (K-M) stars but increase towards earlier spectral types, and ≲0.2 in $\log(L_*/L_\odot)$ at all spectral types. Two luminosities are plotted for all stars later than M7, with the asterisk indicating the luminosity calculated assuming the star has the $V-I$ color and bolometric correction of an M7 star; see text. Superimposed are the zero-age main sequence and the pre-main sequence evolutionary tracks of D'Antona & Mazzitelli (1994, model 1); over the mass range from 0.1 $M_\odot$ to 2.5 $M_\odot$; Swenson *et al.* (1994, model F) from 3 $M_\odot$ to 5 $M_\odot$; and Iben & Cameron (1967) from 10 $M_\odot$ to 50 $M_\odot$. The apparent trend of increasing stellar age with mass suggests errors in the zero point of the pre-main-sequence evolutionary tracks, i.e., the initial mass-radius relationship with which the calculations begin.

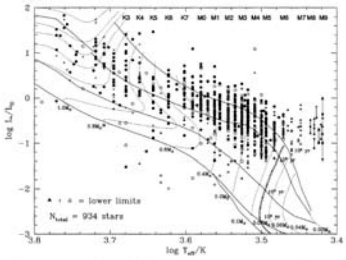


FIG. 13. *Low-mass end of the HR diagram for the Orion Nebula Cluster.* All lines and symbols are the same as in Fig. 12, with the pre-main sequence evolutionary calculations of D'Antona & Mazzitelli now shown down to 0.02 $M_\odot$. The hydrogen-burning mass limit of 0.08 $M_\odot$ is emphasized. The temperature-spectral-type relationship over the range from K3–M9 is denoted. Note the locations of stars M6.5 and later relative to the tracks. These are probably young brown dwarfs. For a magnitude-limited sample restricted to $I_C$<17.5 mag, our data begin to become incomplete at ages older than 1 Myr and masses less than 0.1 $M_\odot$, assuming a typical extinction of $A_V$=2 mag.

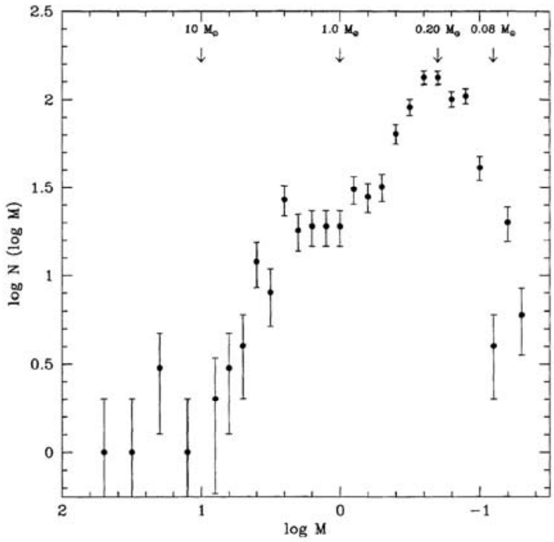


FIG. 17. *The Initial Mass Function as measured in the Orion Nebula Cluster.*

Hillenbrand 1997, AJ, 113, 1733



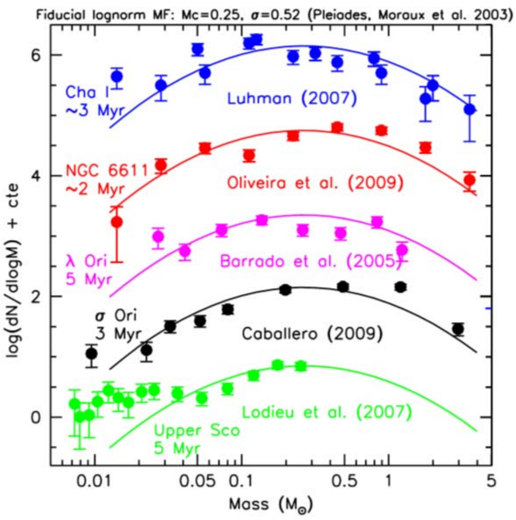


**Fig. 9.** The IMF determined in a number of young (< 10 Myr) clusters and star forming regions (offset for clarity). The solid lines show the log-normal model that best fits the Pleiades (see Fig. 8). The MFs may be generally consistent with that of the Pleiades but the MF of Upper Sco is quite different. Figure constructed by Bouvier & Moraux.

Jeffries 2012

## Stellar Initial Mass Function and Dense Core Mass Function

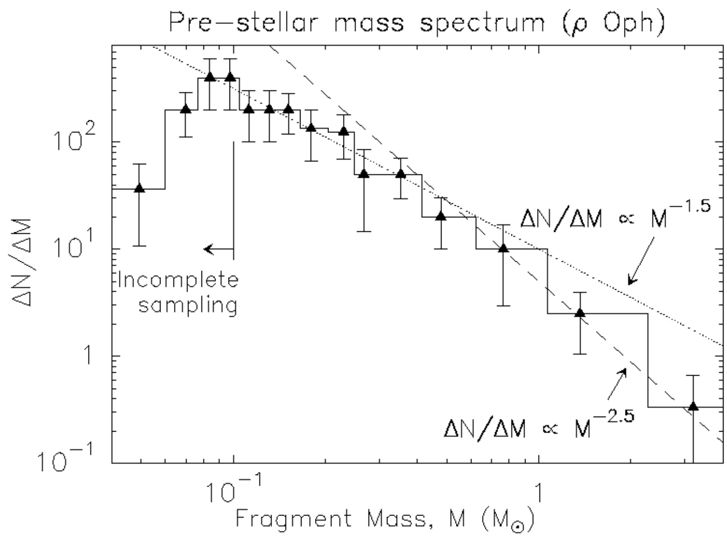


Andre et al. (2000) Protostars & Planets IV

91

## Formation of Massive Stars

- **Competitive accretion (of cloud cores)**

  ... low-mass protostars competing with each other, and accrete matter from the parent molecular cloud

- **Coalescence of two or more stars with lower masses**

92

SUBMITTED ON FEBRUARY 17TH, 2015
Preprint typeset using LATEX style emulateapj v. 12/16/11



# THE HIGH-MASS STELLAR INITIAL MASS FUNCTION IN M31 CLUSTERS*

DANIEL R. WEISZ[1,12], L. CLIFTON JOHNSON[1], DANIEL FOREMAN-MACKEY[2], ANDREW E. DOLPHIN[3], LORI C. BEERMAN[1], BENJAMIN F. WILLIAMS[1], JULIANNE J. DALCANTON[1], HANS-WALTER RIX[4], DAVID W. HOGG[2,4], MORGAN FOUESNEAU[4], BENJAMIN D. JOHNSON[5], ERIC F. BELL[6], MARTHA L. BOYER[7], DIMITRIOS GOULIERMIS[4,8], PURAGRA GUHATHAKURTA[9], JASON S. KALIRAI[7], ALEXIA R. LEWIS[1], ANIL C. SETH[10], EVAN D. SKILLMAN[11]

*Submitted on February 17th, 2015*

## ABSTRACT

We have undertaken the largest systematic study of the high-mass stellar initial mass function (IMF) to date using the optical color-magnitude diagrams (CMDs) of 85 resolved, young (4 Myr $< t <$ 25 Myr), intermediate mass star clusters ($10^3$-$10^4$ $M_\odot$), observed as part of the Panchromatic Hubble Andromeda Treasury (PHAT) program. We fit each cluster's CMD to measure its mass function (MF) slope for stars $\gtrsim 2\ M_\odot$. By modeling the ensemble of clusters, we find the distribution of MF slopes is best described by $\Gamma = +1.45^{+0.03}_{-0.06}$ with a very small intrinsic scatter. This model allows the MF slope to depend on cluster mass, size, and age, but the data imply no significant dependencies within this regime of cluster properties. The lack of an age dependence suggests that the MF slope has not significantly evolved over the first $\sim 25$ Myr, and provides direct observational evidence that the measured MF represents the IMF. Taken together, this analysis — based on an unprecedented large sample of young clusters, homogeneously constructed CMDs, well-defined selection criteria, and consistent principled modeling — implies that the high-mass IMF slope in M31 clusters is universal. The IMF has a slope ($\Gamma = +1.45^{+0.03}_{-0.06}$) that is slightly steeper than the canonical Kroupa (+1.30) and Salpeter (+1.35) values, with no drastic outliers in this sample of nearly 100 clusters. Using our inference model on select Milky Way (MW) and LMC high-mass IMF studies from the literature, we find $\Gamma_{MW} \sim +1.15 \pm 0.1$ and $\Gamma_{LMC} \sim +1.3 \pm 0.1$, both with intrinsic scatter of $\sim$0.3–0.4 dex. Thus, while the high-mass IMF in the Local Group may be universal, systematics in literature IMF studies preclude any definitive conclusions; homogenous investigations of the high-mass IMF in the local universe are needed to overcome this limitation. *Consequently, the present study represents the most robust measurement of the high-mass IMF slope to date*. To facilitate practical use over the full stellar mass spectrum, we have grafted the M31 high-mass IMF slope onto widely used sub-solar mass Kroupa and Chabrier IMFs. The increased steepness in the M31 high-mass IMF slope implies that commonly used UV- and H$\alpha$-based star formation rates should be increased by a factor of $\sim$1.3–1.5 and the number of stars with masses $> 8\ M_\odot$ are $\sim 25\%$ fewer than expected for a Salpeter/Kroupa IMF.

93